A Novel Approach to Hugoniot Measurements Utilizing Transparent Crystals

D. E. Fratanduono, J. H. Eggert, M. C. Akin, R. Chau, N. C. Holmes

Disclaimer

This document was prepared as an account of work sponsored by an agency of the United States government. Neither the United States government nor Lawrence Livermore National Security, LLC, nor any of their employees makes any warranty, expressed or implied, or assumes any legal liability or responsibility for the accuracy, completeness, or usefulness of any information, apparatus, product, or process disclosed, or represents that its use would not infringe privately owned rights. Reference herein to any specific commercial product, process, or service by trade name, trademark, manufacturer, or otherwise does not necessarily constitute or imply its endorsement, recommendation, or favoring by the United States government or Lawrence Livermore National Security, LLC. The views and opinions of authors expressed herein do not necessarily state or reflect those of the United States government or Lawrence Livermore National Security, LLC, and shall not be used for advertising or product endorsement purposes.

A Novel Approach to Hugoniot Measurements Utilizing Transparent Crystals

D. E. Fratanduono, J. H. Eggert, M. C. Akin, R. Chau, N.C. Holmes

A new absolute equation of state measurement technique is described and demonstrated measuring the shock state and the refractive index of MgO up to 226 GPa. This technique utilizes steady shock waves and the high-pressure transparency of MgO under dynamic shock compression and release. Hugoniot measurements performed using this technique are consistent with previous measurements. A linear dependence of the shocked refractive index and density is observed up to 226 GPa, over a magnitude greater in pressure that previous studies. The transparency of MgO along the principal Hugoniot is higher than any other material reported to date. We observe a significant change in the refractive index of MgO as the Hugoniot elastic limit is exceeded due to the transition from uniaxial to hydrostatic strain. Measurements of the elastic-plastic two-wave structure in MgO indicate a nucleation time for plastic deformation.

I. Introduction

The equation of state (EOS) of material in the warm dense matter (WDM) regime is of significant importance to many branches of science[1] (i.e. astrophysics, geophysics, plasma physics, inertial confinement fusion…). Several techniques have been developed to measure the EOS of materials[2-4] at high pressure in order to provide substantial experimental data to construct EOS models and tables. Among these techniques, only dynamic experiments are able to measure absolute stress-density without relying on any

standard. Of special note are absolute Hugoniot methods that trace a unique path through phase space defined by simple conservation laws.

Four classes of techniques have been developed that absolutely measure the principal Hugoniot: symmetric-impact experiments[3,5-7], radiography experiments[8,9], gamma-active reference layers[10] and Doppler shifts of resonance peaks[11]. Symmetric-impact experiments using both single-stage and two-stage gas guns have dominated due to their high-precision and experimental ease, when compared to other techniques. In this work, we demonstrate a new technique for absolute Hugoniot measurements using transparent materials. We present absolute Hugoniot measurements deduced from optical phenomena corresponding to the entrance and exit of a transparent shock within an MgO window.

This new technique is demonstrated using MgO for multiple reasons. Firstly, the stability of the MgO B1 structure at high pressure is unique and suggests that MgO is well suited to be used as an equation of state standard and transparent optical window.[12] Secondly, MgO is important to the geophysical community, as it is a major constituent of the earth and other rocky planets. The physical properties of MgO in the warm dense matter regime are essential in geophysical models[13-15]. Thirdly, MgO has been the focus of numerous high-pressure static[16-21] and dynamic compression experiments[12,22-24]. The principal Hugoniot has been measured to 199 GPa making it an excellent transparent crystal to examine the experimental technique proposed herein. Lastly, to date few transparent crystals (e.g. LiF,[7,25-28] PPMA,[29] Quartz,[31] Fused Silica and Sapphire[30]) have been investigated under shock compression. Along the principal Hugoniot, the highest shock refractive index measurements reported is 115 GPa for LiF. Discovering a new crystal that remains transparent to higher pressure with higher shock impedance than LiF will advance *in-situ* dynamic measurements. This paper is outlined as follows. In Section

2

(II) the theory is presented followed by the experimental technique in Section (III). The results and a discussion are provided in Section (IV) and the conclusions are presented in Section (V).

II. Theory

a. Single Wave Analysis

Setchell[30] first showed that for optical observations of a steady shock the refractive index is expressed as

$$n_S = \frac{U_{App} - D\, n_o}{U_{True} - D},\qquad (1)$$

where U_{App} is the observed *apparent* particle velocity, D is the shock velocity, U_{True} is the *true* particle velocity, and n_o is the unshocked refractive index at the probe frequency ($n_o = 1.7147$ for this study). The *apparent* particle velocity differs from the *true* particle velocity due to the varying optical path length of the window. Fratanduono *et al.*[28] later showed that the arrival of a transparent shock at the free surface of an optical window results in a discontinuity in the *apparent* velocity profile defined as ΔU_{BO}. Upon shock breakout, the shocked refractive index is

$$n_S = \frac{\Delta U_{BO} + 2D\, n_o - U_{FS}}{2D - U_{FS}},\ (2)$$

where U_{FS} is the free surface velocity of the window.

For steady shocks within the optical window, the refractive index defined by Equations (1) and (2) are equivalent. The *true* particle velocity is

$$U_{True} = \frac{-DU_{FS} + Dn_oU_{FS} + 2DU_{App} - U_{FS}U_{App} + D\Delta U_{BO}}{2Dn_o - U_{FS} + \Delta U_{BO}}.\qquad (3)$$

In this work, U_{App}, U_{FS}, and ΔU_{BO} are measured directly using PDV. The shock velocity (D) is determined from the measured sample thickness and shock transit time. From these parameters, the *true* particle velocity $U_{(True)}$ and the shocked refractive

index (n_s) are determined using Equations (3) and (2), respectively. This technique requires steady shocks within the optical window but *does not require impedance matching*.

To illustrate these parameters, the measured velocity profile of shot 4108 is shown in Figure (1A). The refractive index profiles prior to and after the shock breakout are shown in Figure (1B) and Figure (1C), respectively. Prior to shock breakout ($t =$ 31.3 ns) the *apparent* particle velocity (U_{App}) is measured using PDV. At shock breakout, a discontinuity in the *apparent* velocity is observed and defined as ΔU_{BO}. After shock breakout, the free surface (U_{FS}) is no longer stationary and is measured using PDV.

b. Elastic-Plastic Two-Wave Structure

For the special case of an elastic-plastic two-wave structure within an optical window, Equations (1), (2) and (3) are not valid. Define the leading elastic wave as D_E and trailing plastic wave D_P, where subscripts E and P refer to the elastic and plastic waves, respectively. Equation (1) becomes

$$n_{S_P} = \frac{U_{App,P} - D_P n_o + (D_E - D_P)(n_{S_E} - n_o)}{U_{True,P} - D_P}, \quad (4)$$

where $U_{App,P}$ is *apparent* velocity observed when the probe passes through both the elastic and plastic waves, the n_{S_E} is the refractive index of the elastic, n_{S_P} is the refractive index of the plastic waves, and $U_{True,P}$ is the particle velocity behind the plastic wave.   Define $U_{True,E}$ to be the particle velocity behind the elastic wave. Equation (2) is valid for the arrival of the elastic wave (D_E) at the window free surface and becomes

$$n_{S_E} = \frac{\Delta U_{BO_E} + 2 D_E n_o - U_{FS_E}}{2 D_E - U_{FS_E}}, \quad (5)$$

where ΔU_{BO_E} is the observed discontinuity when the elastic wave breaks out of the sample and U_{FS_E} is the free surface velocity after the elastic breakout. The velocity of the elastic wave (D_E) is determined from the measured transit time (Δt_E) and sample thickness (L). Equation (3) is not valid for the arrival of the plastic wave at the free surface for two reasons. Firstly, the derivation of Equation (3) assumes that the free surface is stationary. Secondly, the velocity of the plastic wave at shock breakout is increased due to the interaction of the plastic wave with the release of the elastic wave. Define D_{PE} to be the velocity of the plastic wave after interaction with the elastic release fan. Accounting for these effects, the refractive index of D_{PE} at shock breakout is

$$n_{S_{PE}} = \frac{\Delta U_{BO_{PE}} + 2D_{PE}\, n_o - U_{FS_{PE}} - U_{FS_E}(n_o - 1)}{2D_{PE} - U_{FS_{PE}}}, \qquad (6)$$

where $U_{FS_{PE}}$ is the free surface velocity and $\Delta U_{BO_{PE}}$ is the observed discontinuity when D_{PE} arrives at the free surface.

It is important to note that the shock density of $\rho_{S_{PE}}$ is not the same as ρ_{S_P}. For the plastic wave D_P, the material ahead of the wave corresponds to the elastic state. The density of the plastic wave is defined as

$$\rho_{S_P} = \rho_{S_E} \frac{D_P - U_{True,E}}{D_P - U_{True,P}}. \qquad (7)$$

The moment before D_{PE} arrives at the free surface of the sample assume that the density ahead of the shock front is ρ_o and the particle velocity is $U_{True,E}$. Therefore, the density of the D_{PE} at breakout is defined as

$$\rho_{S_{PE}} = \rho_o \frac{D_{PE} - U_{True,E}}{D_{PE} - U_{True,PE}}, \qquad (8)$$

For a single wave, the *true* particle velocity is determined from the equivalence of Equation (1) and Equation (2). However for the special case of a two-wave structure, the refractive index defined by Equation (4) and Equation (5) are *not* equal. Therefore,

5

assume that the measured free surface velocity is approximately twice the *true* particle velocity: $U_{True,E} = U_{FS_E}/2$ and $U_{True,PE} = U_{FS_{PE}}/2$. In addition, D_{PE} is approximated by

$$D_{PE} = D_E + U_{FS_E}, \tag{9}$$

which assumes that the material is perfectly elastic prior to the arrival of the second wave[31-33] and that the elastic release fan can be approximated by a single wave. This assumption is valid since the sound speed of material below the Hugoniot elastic limit is nearly constant for most materials. The velocity of the plastic shock[33] is

$$D_P = \frac{(\Delta t_P - \Delta t_E)(2D_E U_{True,E} - 2U_{True,E}^2 - D_{PE}D_E + D_{PE}U_{True,E}) + L(D_E - U_{True,E} + D_{PE})}{\Delta t_P(D_{PE} - 2U_{True,E}) + \Delta t_E(U_{True,E} + D_E)}, \tag{10}$$

where Δt_E is the transit time of the elastic wave, Δt_P is the observed transit time of the plastic wave and L is the length of the window.

The measured velocity profiles for the two wave structure experiments are shown in Figure (2) for shot 4081. At $t = 0$, the shock enters the MgO window from an aluminum pusher. The *apparent* velocity (blue dashed lines) corresponds to the elastic wave and the refractive index profile is shown in Figure (2B). As discussed in Section IV, a delay in the onset of plastic deformation is observed. The plastic wave emerges at 1.8(±0.2) ns and an increase in the *apparent* velocity is observed (solid blue line). The corresponding refractive index profiles at this time are shown in Figure (2C). It is important to note that between 1.8(±0.2) ns and 54.1 (±1.1) ns the observed *apparent* particle velocity is constant. We cannot discern decay in the elastic-wave particle velocity, which suggest the refractive index of the elastic-wave is linear with respect to density[27,34] or the variation in the refractive index is small.

At 54.1 (±1.1) ns, the elastic wave arrives at the window free surface. A discontinuity in the *apparent* velocity is observed (dashed blue line) and the free-surface

6

velocity is measured (dashed red line). Between 54.1 ($\pm$1.1) ns and 58.0 ($\pm$1.9) ns, complex wave interactions occur between the plastic wave front and the reflected elastic limit. The complex wave interactions between the reflected elastic-wave and the plastic wave are not indicated in Figure (2D). As discussed above, the velocity of the plastic wave after interaction with the elastic release fan is approximated as D_{PE}. At 58.0 ($\pm$1.9) ns D_{PE} arrives at the free surface and a second discontinuity in the *apparent* velocity is observed (solid blue line), and the free surface is accelerated (solid red line). For late times ($t \gg 58.0$ ns), an approximate refractive index profile is shown in Figure (2E).

To determine the *true* particle velocity of the plastic wave assume that $n_{S_{PE}}$ is a small deviation of n_{S_P} or

$$n_{S_{PE}} = n_{S_P} - \varepsilon, \tag{11}$$

where $\varepsilon \ll n_{S_P}$. The *true* particle velocity of the plastic wave ($U_{True,P}$) is determined from Equation (4) and Equation (11). The *true* particle velocity of the plastic wave is

$$U_{True,P} = D_P + \frac{U_{App,P} - D_P n_o + (D_E - D_P)(n_{S_E} - n_o)}{n_{S_{PE}} + \varepsilon}. \tag{12}$$

As shown in Section (III), the shocked refractive index of MgO of the plastic wave is linear with density,

$$n_s = a + b\rho_s, \tag{13}$$

where coefficient a and b are determined by fitting to experimental data. An estimate for ε is determined from

$$\varepsilon = b(\rho_P - \rho_{PE}). \tag{14}$$

The elastic-plastic Hugoniot measurements are extracted using our knowledge of the variation of the plastic refractive index with density. This requires an estimate of b which is determined from the high-pressure (>97 GPa) single plastic wave data, $b =$

$-0.200(\pm0.003)$. The *true* particle velocity of the plastic wave, defined in Equation (12), depends upon the parameters, n_o, U_{App}, D_P, D_E, n_{S_E}, $n_{S_{PE}}$ and ε. n_o *is* the refractive index of the MgO window at ambient conditions and is known. U_{App} and D_E are directly measured using PDV. D_P, n_{S_E}, $n_{S_{PE}}$ are determined from Equations (10), (5) and (6), respectively. ε is determined from the high-pressure single-wave plastic refractive index measurements and Equations (7), (8), (9) and (14).

III. Experimental Technique

Strong steady shocks are generated using Lawrence Livermore National Laboratory's (LLNL's) two-stage light gas gun.[35] The technique describe herein, was examined by through symmetric impact experiments using flyer plates and baseplates of the same material (aluminum or tantalum) with MgO samples affixed to the rear surface. The flyer plate and baseplate densities are within less than 0.05% uncertainty (2.71 g/cc and 16.65 g/cc for aluminum and tantalum, respectively). The results obtained using this technique are compared with impedance matching results. The linear fits to the shock velocity versus particle velocity relationships used in this study are $D = 5.45(\pm0.05) + 1.324(\pm.016)U_{True}$ for aluminum[36] and $D = 3.293(\pm0.005) + 1.307(\pm0.025)U_{True}$ for tantalum.[37]

Transparent MgO windows, with density of 3.58 g/cc and the crystal axis oriented <100>, are affixed to the rear surface of the baseplate. Sample densities are in close agreement (< 1%) with standard values. The Hugoniot measurements determined using this technique are compared with results obtained through impedance matching the baseplate Hugoniot with the MgO Hugoniot. The MgO Hugoniot used for comparison is $D = 6.61(\pm0.05) + 1.36(\pm0.02)U_{True}$ taken from the work of Vassiliou and Ahrens.[22]

The flyer-plate dimensions are 1.5 mm thick and 25.7 mm in diameter. The projectile velocities are measured to better than 1% accuracy using a flash radiographic system.[35] The base plate thickness is 2.0 mm. The MgO thickness varied between ~0.3 mm and ~1.0 mm and are 5.0 mm square. Baseplate and window thicknesses are chosen to prevent edge releases and projectile release waves from occurring during the experiment duration. MgO windows are flash coated with ~0.1 μm of silver and are glued to the baseplate. In addition, MgO/MgO sandwich targets with an *in situ* silver layer are also attached to the baseplate in some experiments. The measured glue thickness is less than ~3 μm in all experiments. A conceptual drawing of the target design is shown in Figure (3) with two different MgO packages. The top half of Figure (3) illustrates measurements made at the pusher/MgO interface. The bottom half indicates *in situ* MgO/MgO interface measurements.

These experiments were designed such that multiple transparent crystals were studied simultaneously. In addition to MgO, other samples studied were MgF_2, CaF_2, KBr, CsI, KCl and NaCl. Of those materials, MgO remained transparent to the highest pressure and a single phase was observed, indicating it is well suited as an optical window. The other materials studied are not well suited since they were observed to become opaque at lower pressures than MgO or complex wave structures were observed. The Hugoniot and refractive index measurements of MgF_2, CaF_2, KBr, CsI, KCl and NaCl will be published at a later time.

PDV[26,38] is used to measure the experimental velocities. PDV is a heterodyne velocimetry technique that combines Doppler shifted and unshifted laser light. The interference of the two signals creates a beat frequency that is proportional to the velocity of reflected probe beam surface. LLNL's PDV system utilizes 1550 nm (FWHM < 1 nm) laser light from a single-mode optical fiber with power output of 0.200 W. The

9

interference signal is measured using an infrared detector recorded with high bandwidth (8-20 GHz) digitizers. Laser light is coupled to the target using probes with focal lengths of 10 mm and a beam diameter of ~30 μm at 10 mm working distance. The numerical aperture of the fibers is 0.11 with a cone angle of ~7°. Probes have normal-incidence polished fiber end face with a -15 dB (3 %) back reflection. Best contrast single is achieved when the reflection surface is matched with the probe reflection. The MgO optical windows are roughened to reduce the signal sensitivity to tilt. The probe alignment is preformed using a back-reflection meter to ensure proper focusing at the MgO interface. The infrared returned optical signals are converted to electrical signals using Mytek optical receivers. Signals are recorded using high-bandwidth Tektrornix oscilloscopes with time base accuracy of 2 ppm. The measured frequency is converted to velocity through a Wigner transform. The width of the transform is directly related to the uncertainty relation ($\Delta t \Delta U$). Smaller widths increase the temporal resolution (Δt) while decreasing the certainty in the velocity (ΔU) and vice-versa.

As discussed by Jensen *et al.*[26] the uncertainty in the PDV velocity is limited by the duration of constant velocity in the experiment. Uncertainties in the probe wavelength, probe orthogonality and digitizer time calibration are significantly less than uncertainties determined using the Wigner transform. For signals in which the velocity is constant over numerous transform windows, the uncertainty in the measured velocity is <1%. For signals that are of the order of a few beats, the uncertainty in velocity is larger and is determined by the ability to resolve the velocity using the Wigner Transform. Transit times are determined from the raw frequency data by determining the sudden change in beat frequency. Uncertainties in the timing determined in this technique are

assumed to be no better than ½ the time of a single period (~100 ps), which is significantly greater than the time base accuracy of the oscilloscopes.

IV. Results and Discussion

The Results and Discussion Section is divided into three parts. The single wave analysis is discussed in Subsection (a), the elastic-plastic two-wave results in Subsection (b) and the refractive index measurements are summarized in Subsection (c)

a. Single Wave Results (Plastic Deformation)

Four experiments are conducted above the elastic-plastic transition in MgO where the HEL is over driven and a single wave is observed. The measured parameters for the single shock case are shown in Table (1). The experimental results determined using the analysis technique discussed in Section (IIa) are summarized in Table (2). Table (2) compares the results obtained using this technique with the results obtained through impedance matching the baseplate and MgO. Measurements of the particle velocity using Equation (3) are within <1% values obtained using conventional impedance matching. In addition, a single experiment is performed where simultaneous measurements are taken at the Ta/MgO interface and compared to measurements taken within an MgO/MgO "sandwich" target as indicate in Figure (3). Those results are within 0.2% agreement indicating that the results are independent of the interface material.

A plot of the shock velocity vs. *true* particle velocity is shown in Figure (4). The results obtained using the Equation (3) are shown as red circles with error bars and are compared with previously published results.[12,22-24] The refractive index versus density is shown in Figure (5). These results (red circles) are compared to values obtained using impedance matching and Equation (1) (grey diamonds) and Equation (2) (black squares). The observed agreement validates this technique. For shots s4075 and s4092, comparable uncertainties between previous impedance matching[12,22-24] and these results

are observed. It is important to note, that the Hugoniot measurements determined here are absolute where previous measurements required impedance match standards (aluminum or tantalum).

Although the uncertainties of these results are comparable with impedance matching, their precision would exceed the precision of measurements determined using a symmetric impact. For both symmetric impact and the technique outline here, the shock velocity is determined through time of flight and the uncertainties are equivalent. The uncertainty in the particle velocity is greater using the technique proposed here compared to the symmetric impact experiment. Symmetric impact experiments determine the particle velocity from the measured flyer-plate velocity at impact ($U_{True} = U_{Flyer}/$ 2). The uncertainty in the particle velocity is one half the uncertainty in the flyer-plate velocity.   The particle velocity determined using this technique is determined from Equation (3).   This requires four measurable parameters (D, U_{App}, U_{FS}, ΔU_{BO}) whose uncertainties are comparable to that of the flyer-plate velocity. Therefore, the uncertainty using this technique is greater than that of symmetric impact experiments. An important assumption for symmetric impact experiments is that the state of the flyer-plate at impact is known. If the flyer plate is preheated, a systematic uncertainty is introduced, when assuming standard conditions at impact. The technique proposed here requires no knowledge of the flyer-plate. Thus, this technique enables experimental examination of the flyer-plate conditions at impact.

Previously, it was postulated[23] that MgO undergoes a phase transition at 170+/-10 GPa due to a 1.9% density collapse due to the slight "kink" in the shock velocity versus *true* particle velocity at ~12 μm/ns. The density collapse proposed may generate a two-wave structure in the wave profiles that could be observed when the shock breaks out of

the optical window. In this work, a two-wave structure between pressures of 97 to 226 GPa was not observed which may not support the claims of Zhang *et al.*[23] These results suggest that the B1 structure is maintained up to ~226 GPa.

b. Elastic-Plastic Two-Wave Structure

Two experiments are performed in which the Hugoniot elastic limit is not over driven. A summary of the experimental parameters is provided in Table 3. The velocity of the elastic wave is measured to be 9.7(±0.2) μm/ns and is in agreement with ultra-sonic measured value[21] of 9.696 μm/ns. The Hugoniot measurements are shown in Figure (4) as red and blue triangles for the plastic and elastic wave, respectively. The Hugoniot measurements are in agreement with previous results. A weighted orthogonal fit[39] is shown in Figure (4) (excluding the elastic-wave data) as the black dashed line. Uncertainties were not quoted with the data published by Carter *et al.*[24] We have assumed uncertainties of 1% in both shock velocity and particle velocity; the typical uncertainty in gas-gun experiments. The orthogonal fit is $D = 9.21(\pm0.02) + 1.35(\pm0.02)(U_{True} - 1.91$ or $D = 6.64 \pm 0.04 + 1.35 \pm 0.02 U_{True}$ in linear form.

Refractive index measurements are shown in Figure (5) as red and blue triangles for the plastic and elastic wave, respectively. Figure (5) compares the refractive index values determined using this technique and the results determined from impedance matching. The impedance matching results using Equations (1) and (2) have neglected the two-wave structure; ΔU_{BO} is taken to be the sum of ΔU_{BO_E} and $\Delta U_{BO_{PE}}$. These values, which contain a systematic uncertainty, are in good agreement with the values obtained using the technique presented here suggesting that the refractive index of the elastic wave has a small affect on the measured *apparent* particle velocity.

The most striking results from the measured load-surface wave profile are that the elastic and plastic waves do not originate at the same time, as shown in Figure (2). For both experiments where the elastic-plastic transition is observed, a delay in the emergence of the plastic wave is observed (1.8(+/-0.2) ns and 4.9(+/- 0.2) ns for shock pressures of 56.4(+/- 2.0) GPa and 38.4 (+/- 1.6) GPa, respectively). This suggests a nucleation time for the plastic wave, consistent with theoretical and experimental works.[40-42] Our interpretation of the data is that the first wave to emerge corresponds to the impedance matching of the baseplate with a linear extrapolation of the elastic Hugoniot, illustrated in Figure (6) as the intermediate point (I). After nucleation occurs, the MgO deforms plastically and a plastic wave emerges that correspond to the intersection of the baseplate Hugoniot and the MgO plastic Hugoniot, plastic point (P). The particle velocity behind the elastic wave decays with propagation distance, to elastic point (E), as shear stress is relieved. These claims are corroborated with our understanding of the optical path length within the window. Consider the case illustrated in Figure (6). The refractive index at point (I) can be determined before the plastic wave emerges using Equation (1). This requires impedance matching with the baseplate. As described above, assume that point (I) is determined from the interception of the extrapolated elastic Hugoniot and the baseplate Hugoniot. Using these values and the measured *apparent* velocity, the shocked refractive index is determined. Values are shown in Figure (4) as inverted blue diamonds. These measurements suggest that the variation of the refractive index with density for the elastic wave is nearly constant, consistent with the elastic wave measurements Stevens *et al.*[43] Furthermore, one can show that when the plastic wave emerges, a change in the optical path length results. This is manifested as a sudden change in the observed *apparent* velocity,

$$U_{App,P} - U_{App,I} = D_P(n_I - n_P) + n_P U_{True,P} - n_I U_{True,I}, \qquad (15)$$

where $U_{App,I}$ is the *apparent* velocity of the over-driven elastic wave and subscripts I, P and E, denote points in Figure (6). n_I is determined from Equation (1) and impedance matching to determine point (I) in Figure (6). From this derivation, the observed discontinuity is calculated to be 0.38(+/-0.13) μm/ns and 0.33(+/-0.09) μm/ns for shock pressures of 57(+/-2) GPa and 38(+/-2) GPa, respectively. Values are summarized in Table 5. This is in excellent agreement with the measured experimental results of (0.38(+/-0.05) μm/ns) and (0.34(+/-0.03) μm/ns). However, these results cannot discern if the plastic wave emerges from the loading surface or if separation occurs within the bulk.

A single experiment is performed where an Al/MgO and an MgO/MgO interface are measured simultaneously (design shown in Figure (3)). The interface velocity measurements are shown in Figure (7). The red curve is the Al/MgO loading interface and the blue curve is the MgO/MgO bulk interface. For the Al/MgO sample, an over driven elastic wave is observed when the shock first enters the MgO sample. The *apparent* particle velocity is 1.94(+/-0.01) km/s. The second sample consists of an Al baseplate and a sandwiched MgO/MgO sample. For this sample, PDV observes no change in the *apparent* particle velocity when the shock first enters the sample since the probe reflects off an *in situ* layer that is ~500 μm from the MgO loading surface. As the two-wave structure propagates through the MgO window, the particle velocity and pressure behind the elastic wave decays and the two waves separate. When the elastic wave arrives at the *in situ* reflecting layer, the *apparent* particle velocity of the elastic wave has decayed to 0.23(+/-0.1). These measurements are consistent with similar MgO experiments performed by Stevens *et al,*[43] as well as the elastic-wave particle velocity

measurements of other materials.[44-46] As shown in Figure (3A), we do not observe a change in the *apparent* particle velocity as the elastic wave decays. This suggests that the refractive index of the elastic wave is linear in density or the variation in the refractive index with density is small.

c. Refractive Index Measurements

Figure (5) indicates that a linear fit to the plastic wave data does not extrapolate through the elastic wave values or to n_o. The difference in the refractive index values obtained below and above the HEL is attributed to the difference in strain (uniaxial below the HEL and hydrostatic above). Above the HEL, MgO undergoes a loss of shear strength. Deformation of the MgO crystal changes dramatically, resulting in a different refractive index response to increasing pressure. A weighted linear fit to the refractive index to all elastic-shock measurements is

$$n_s = 1.721(\pm 0.043) - 0.002(\pm 0.012)\rho_s . \tag{16}$$

A linear fit to the refractive index of the plastic-wave is

$$n_s = 1.773(\pm 0.016) - 0.020(\pm 0.003)\rho_s . \tag{17}$$

These results suggest that at the elastic limit, a discontinuity in the shocked refractive index is observed.

Previous measurements[43] of the shocked refractive index of MgO at 532 nm are included in Figure (5). Those results did not include uncertainty values for the shocked refractive index. We have reanalyzed those results and assumed a 1% uncertainty in the measure parameters. In addition, the authors noted that the lowest pressure plastic wave measurement had the greatest level of uncertainty and should be "scaled accordingly." We have assumed an uncertainty of two times greater in the measured velocities for this point, as proper values were not published. Those results shows a similar behavior in

that the variation of the shocked refractive index with density for the elastic and plastic-waves when compared to this study.

V. Summary

A new absolute equation of state measurement technique has been described and demonstrated measuring the Hugoniot and refractive index of MgO up to 226 GPa. This technique does not relay upon impedance matching to a standard, does not require knowledge about the flyer plate state at impact or the flyer plate velocity. The Hugoniot measurements performed using this technique are in excellent agreement with previous measurements. A linear dependence of the shocked plastic wave refractive index versus density is observed up to 226 GPa. The high-pressure transparency of MgO indicates that it is well suited to be used as an optical window in interferometry based measurements. These are the highest-pressure shock refractive index measurements reported to date. Lastly, a nucleation time in the emergence of the plastic wave has been observed. After nucleation occurs, the MgO deforms plastically and a plastic wave emerges that correspond to the intersection of the baseplate Hugoniot and the MgO plastic Hugoniot. The unique behavior of the refractive index below and above the Hugoniot elastic limit indicate it is an excellent material to study the phenomena of material strength at this transition.

Reference

1. Committee on High Energy Density Plasma Physics, Plasma Science Committee, and National Research Council, *Frontiers in High Energy Density Physics:The X-Games of Contemporary Science* (The National Academies Press, 2003).
2. G. J. Piermarini and S. Block, Review of Scientific Instruments **46**, 973 (1975).
3. A. H. Jones, W. M. Isbell, and C. J. Maiden, Journal of Applied Physics **37**, 3493 (1966).
4. L.C. Chhabildas and L.M. Barker, Medium: X; Size: Pages: 26, SAND-86-1888 (1986).
5. R. G. McQueen and S. P. Marsh, Journal of Applied Physics **31**, 1253 (1960).
6. C. A. Hall, M. D. Knudson, J. R. Asay, R. Lemke, and B. Oliver, International Journal of Impact Engineering **26**, 275 (2001).
7. D. E. Fratanduono, R. F. Smith, T. R. Boehly, J. H. Eggert, D. G. Braun, and G. W. Collins, Review of Scientific Instruments **83**, 073504 (2012).
8. L. B. Da Silva, P. Celliers, G. W. Collins, K. S. Budil, N. C. Holmes, T. W. Barbee Jr, B. A. Hammel, J. D. Kilkenny, R. J. Wallace, M. Ross, R. Cauble, A. Ng, and G. Chiu, Physical Review Letters **78**, 483 (1997).
9. A. Ravasio, M. Koenig, S. Le Pape, A. Benuzzi-Mounaix, H. S. Park, C. Cecchetti, P. Patel, A. Schiavi, N. Ozaki, A. Mackinnon, B. Loupias, D. Batani, T. Boehly, M. Borghesi, R. Dezulian, E. Henry, M. Notley, S. Bandyopadhyay, R. Clarke, and T. Vinci, Physics of Plasmas **15**, 4 (2008).
10. Ktitorov V.M. Podurets M.A., Trunin R.F., Popov L.V., Matveev A.Ya., Pechenkin B.V., Sevast'yanov A.G, Teplofiz. Vys. Temp. **32**, 952 (1994).
11. C. E. III Ragan, M. G. Silbert, and B. C. Diven, in *Peaceful Nuclear Explosives Meeting* (Vienna, 1976).
12. Thomas S. Duffy and Thomas J. Ahrens, AIP Conference Proceedings **309**, 1107 (1994).
13. Dario Alfè, Physical Review Letters **94**, 235701 (2005).
14. Bijaya B. Karki, Dipesh Bhattarai, and Lars Stixrude, Physical Review B **73**, 174208 (2006).
15. Artem R. Oganov and Peter I. Dorogokupets, Physical Review B **67**, 224110 (2003).
16. Hartmut Spetzler, J. Geophys. Res. **75**, 2073 (1970).
17. Motohiko Murakami, Yasuo Ohishi, Naohisa Hirao, and Kei Hirose, Earth and Planetary Science Letters **277**, 123 (2009).
18. Charles Meade and Raymond Jeanloz, J. Geophys. Res. **93**, 3261 (1988).
19. E. H. Bogardus, Journal of Applied Physics **36**, 2504 (1965).
20. A. E. Gleason, H. Marquardt, B. Chen, S. Speziale, J. Wu, and R. Jeanloz, Geophys. Res. Lett. **38**, L03304 (2011).
21. Yoshio Sumino, Orson L. Anderson, and Isao Suzuki, Physics and Chemistry of Minerals **9**, 38 (1983).
22. M. S. Vassiliou and Thomas J. Ahrens, Geophys. Res. Lett. **8**, 729 (1981).
23. Li Zhang, Zizheng Gong, and Yingwei Fei, Journal of Physics and Chemistry of Solids **69**, 2344 (2008).
24. W. J. Carter, S. P. Marsh, J. N. Fritz, and R. G. McQueen, LA-DC-9990 (1968).

25. J. L. Wise and L. C. Chhabildas, Sandia National Laboratory, Albuquerque, NM, Report SAND-85-0310C, NTIS Order No. DE85015505 (1985).

26. B. J. Jensen, D. B. Holtkamp, P. A. Rigg, and D. H. Dolan, Journal of Applied Physics **101**, 013523 (2007).

27. D. E. Fratanduono, T. R. Boehly, M. A. Barrios, D. D. Meyerhofer, J. H. Eggert, R. F. Smith, D. G. Hicks, P. M. Celliers, D. G. Braun, and G. W. Collins, Journal of Applied Physics **109**, 123521 (2011).

28. D. E. Fratanduono, J. H. Eggert, T. R. Boehly, M. A. Barrios, D. D. Meyerhofer, B. J. Jensen, and G. W. Collins, J. Appl. Phys. **110**, 083509 (2011).

29. L. M. Barker and R. E. Hollenbach, Journal of Applied Physics **41**, 4208 (1970).

30. Robert E. Setchell, Journal of Applied Physics **50**, 8186 (1979).

31. Jerry Wackerle, Journal of Applied Physics **33**, 922 (1962).

32. R. A. Graham and W. P. Brooks, Journal of Physics and Chemistry of Solids **32**, 2311 (1971).

33. Thomas J. Ahrens, W. H. Gust, and E. B. Royce, Journal of Applied Physics **39**, 4610 (1968).

34. Dennis Hayes, Journal of Applied Physics **89**, 6484 (2001).

35. A. C. Mitchell and W. J. Nellis, Review of Scientific Instruments **52**, 347 (1981).

36. P. M. Celliers, G. W. Collins, D. G. Hicks, and J. H. Eggert, J. Appl. Phys. **98**, 113529 (2005).

37. A. C. Mitchell and W. J. Nellis, Journal of Applied Physics **52**, 3363 (1981).

38. O. T. Strand, D. R. Goosman, C. Martinez, T. L. Whitworth, and W. W. Kuhlow, Rev. Sci. Instrum. **77**, 083108 (2006).

39. P.R. Bevington and D.K. Robinson, *Data reduction and error analysis for the physical sciences* (McGraw-Hill, 2003).

40. Y. Partom, Journal of Applied Physics **59**, 2716 (1986).

41. V. Morozov and V. Bogatko, Doklady Physics **53**, 462 (2008).

42. N. Morozov and L. Shikhobalov, Doklady Physics **53**, 529 (2008).

43. G. D. Stevens, L. R. Veeser, P. A. Rigg, and R. S. Hixson, AIP Conference Proceedings **845**, 1353 (2006).

44. John W. Taylor and Melvin H. Rice, Journal of Applied Physics **34**, 364 (1963).

45. William J. Murri and Gordon D. Anderson, Journal of Applied Physics **41**, 3521 (1970).

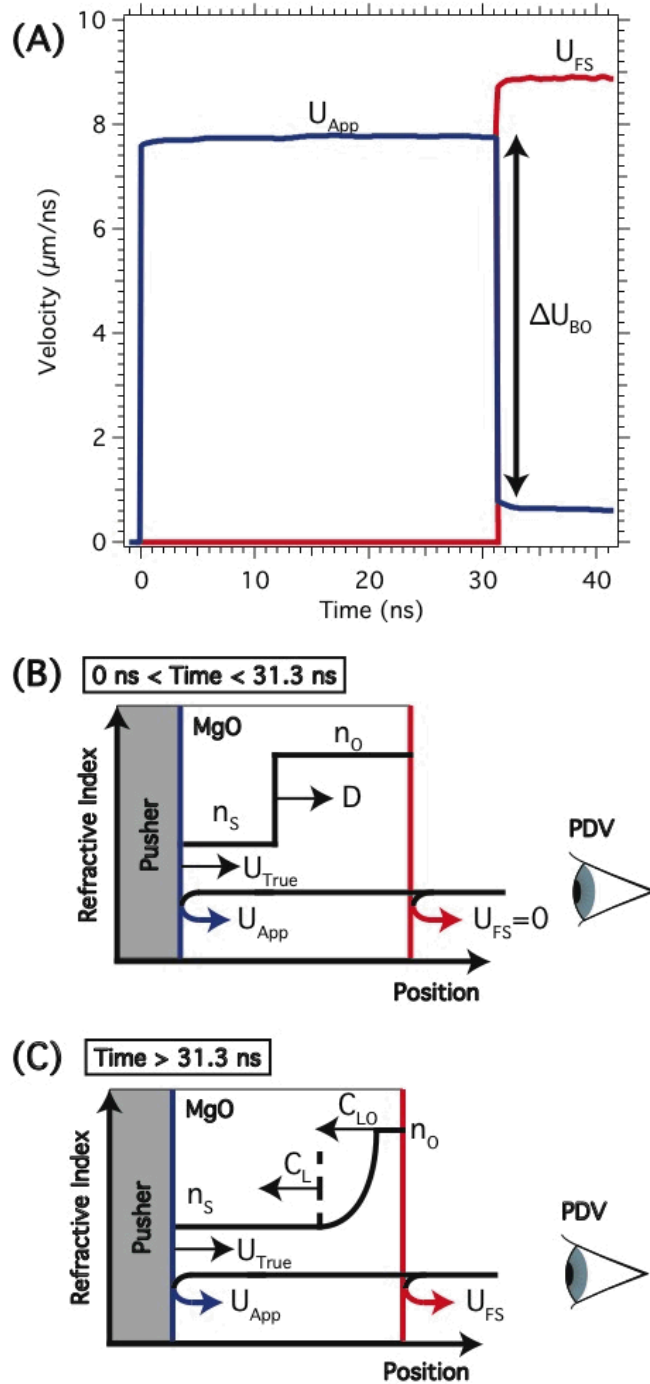46. B. J. Jensen and Y. M. Gupta, Journal of Applied Physics **104**, 013510 (2008).

Figure (1): PDV velocity measurements for single-wave MgO experiments. (A) PDV measurements for shot 4108. The *apparent* velocity is shown in blue and the free surface velocity in red. At 31.3 ns, the shock exists the MgO window and a discontinuity in the *apparent* velocity is observed. (B) The refractive index profiles within the MgO window prior to shock breakout. The Al/MgO interface is shown in blue and the stationary free surface in red. (C) The refractive index profiles within the MgO window after shock breakout. The Al/MgO interface is shown in blue and the free surface in red. The free surface is no longer stationary.
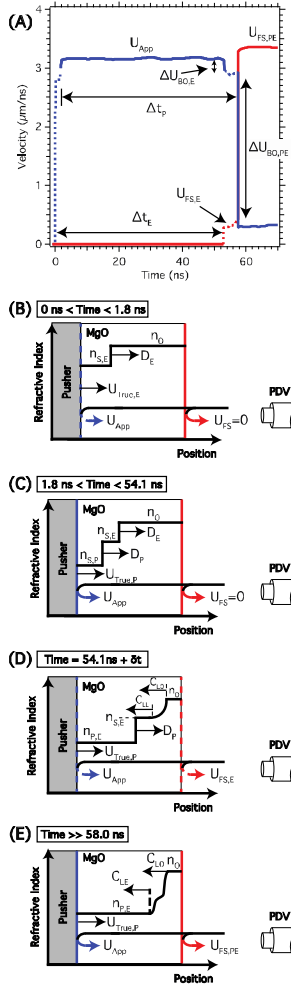
Figure (2): PDV velocity measurements for elastic-plastic two wave experiments. (A) PDV measurements for shot 4081. A 0 ns, the shock enters the MgO sample from an Al pusher. The *apparent* particle velocity of the elastic wave is shown as the dashed blue line. At 1.8 ns, an increase in the *apparent* particle velocity is observed. This corresponds to the formation of the plastic wave (shown in solid blue). At 54.1 ns, the elastic wave arrives at the free surface of the window. A discontinuity in the *apparent* particle velocity is observed (blue dashed line) and the free surface is accelerated (red dashed line). At 58.0 ns, the plastic wave (after interaction with the reflected elastic wave) arrives at the window free surface. This is accompanied with a third discontinuity in the *apparent* particle velocity (solid blue line) and a second discontinuity in the free surface velocity (solid red line). Conceptual refractive index profiles are shown in (B) through (E).
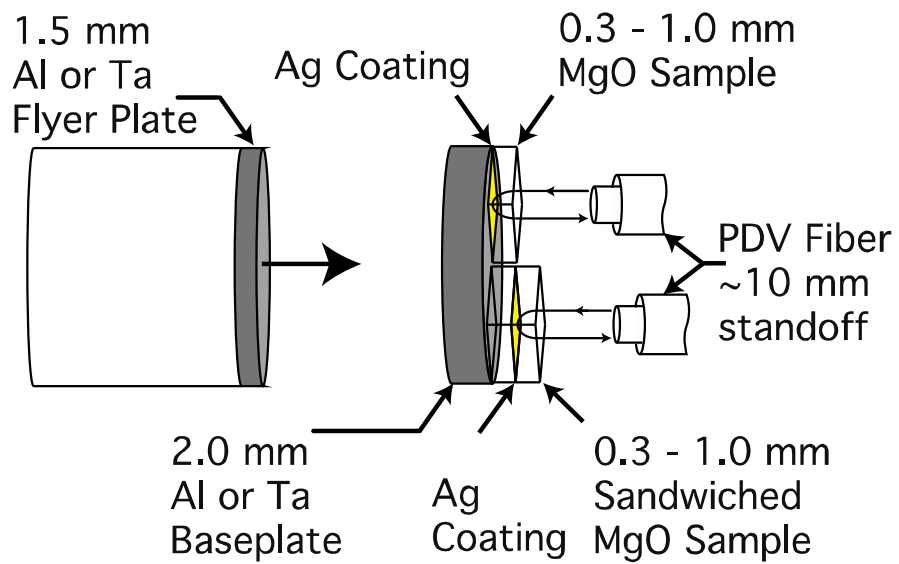
Figure (3): Conceptual target design. The two sample designs used in the study are shown. The top half illustrates the baseplate/MgO loading surface measurements. The bottom half illustrates MgO/MgO *in situ* bulk measurements.
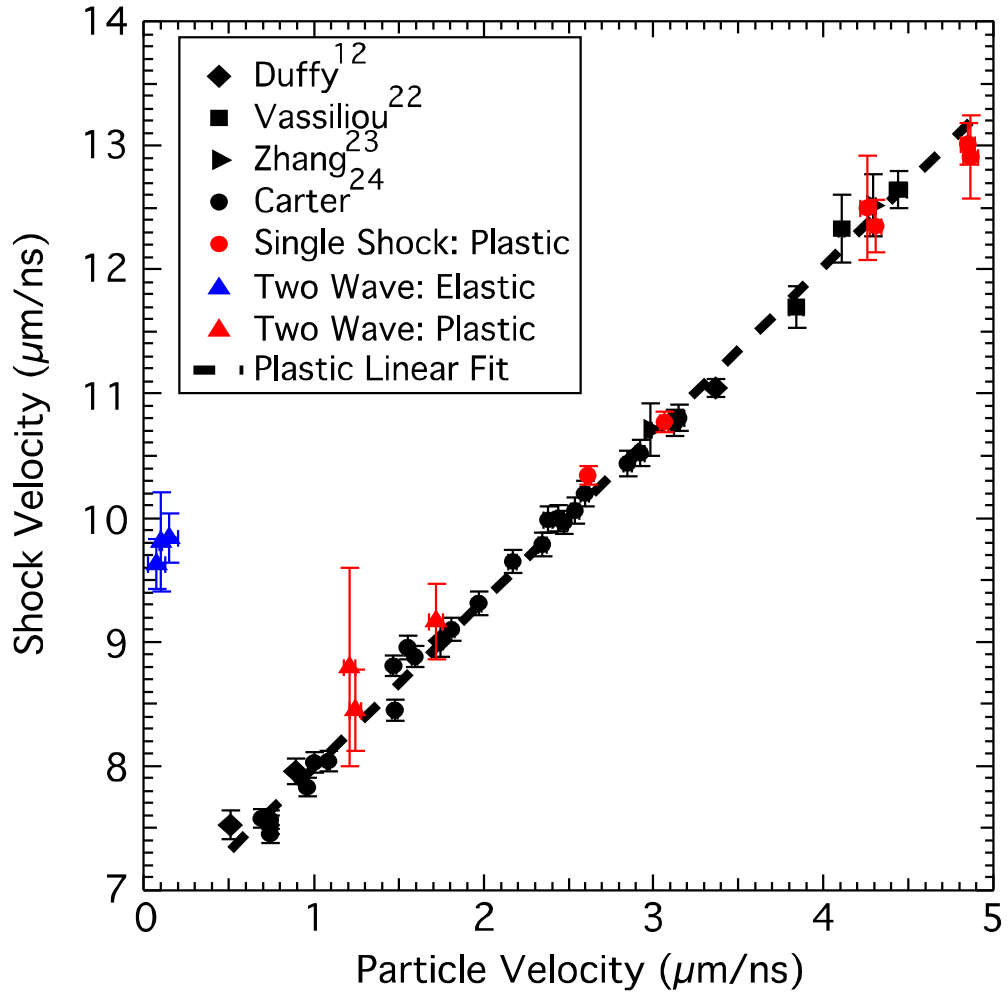
Figure (4): MgO Hugoniot measurements. Previous experimental measurements are shown. The red and blue coloring denotes the elastic and plastic waves, respectively. Single shock wave measurements are shown as red circles and two wave structure measurements are denoted by blue and red triangles. A linear fit to all plastic wave data is shown as the dashed line.
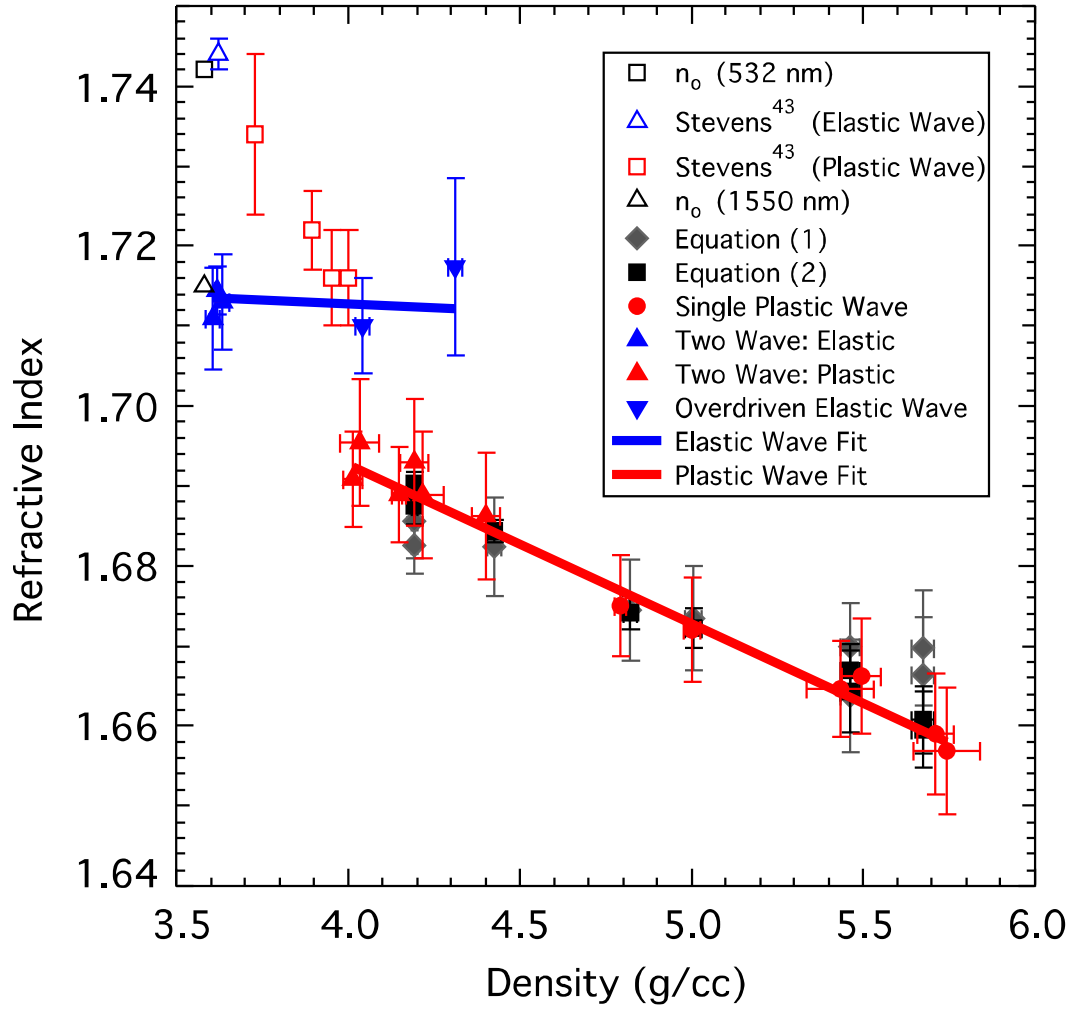
Figure (5): Refractive index versus density. Red and blue colors denote the elastic and plastic waves, respectively. Impedance matching results obtained from Equations (1) or (2) are shown for comparison. The triangles denote the two-wave structure measurements and the circles done the single wave measurements.
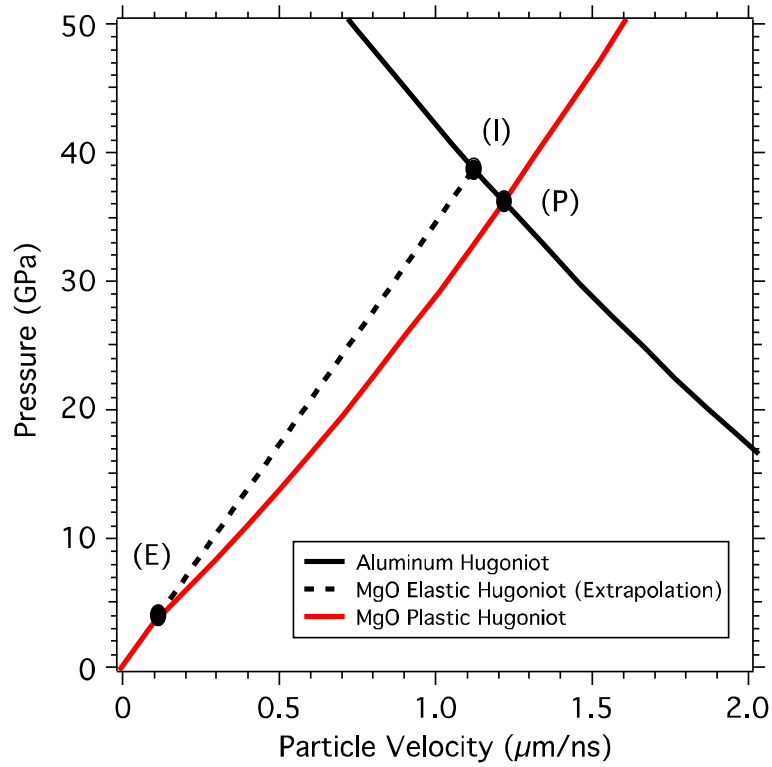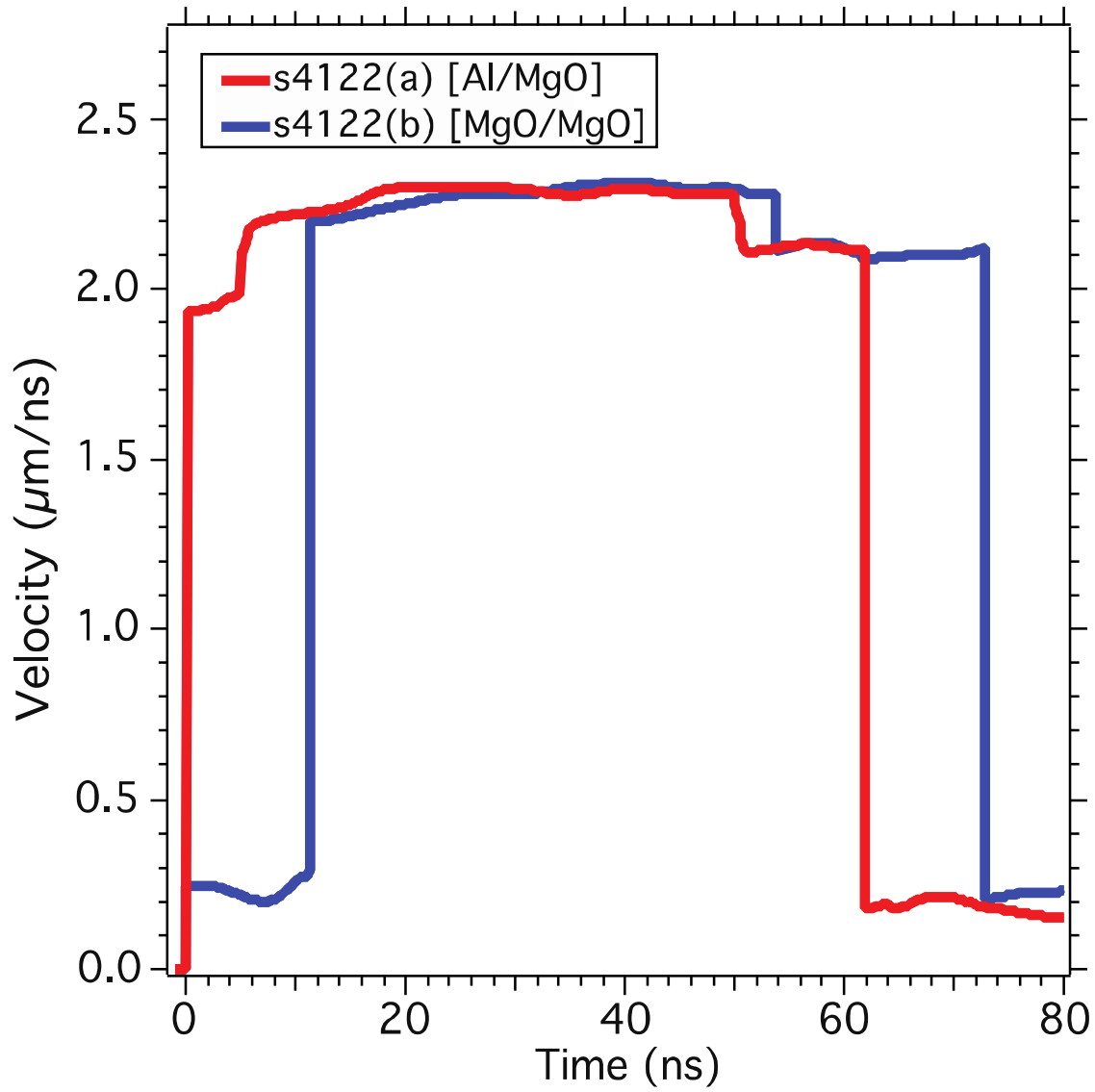
Figure (6): Proposed states corresponding to the MgO elastic-plastic transition. MgO is initially shocked to point (I), an extrapolation of the elastic Hugoniot. After nucleation occurs, a plastic deformation wave emerges from the MgO window, point (P). The particle velocity behind the elastic wave decays with propagation distance to point (E).

Figure(7): Simultaneous interface velocity measurements for an aluminum/MgO The loading surface interface measurement is shown in red and the MgO/MgO *in situ* interface measurement (~500 μm from the MgO loading surface) is shown in blue. Traces have been normalized to the arrival of the elastic wave. The free surface velocity measurements are not show for clarity. The *apparent* particle velocity of the elastic wave is observed to decay with propagation distance into the MgO.

Table 1: Measured parameters for the single shock case.

Shot Number	Baseplate	Interface	Window Length (μm) L	Flyer Plate Velocity (μm/ns) U_{Flyer}	Apparent Velocity (μm/ns) U_{App}	Free Surface Velocity (μm/ns) U_{FS}	Discontinuity at Breakout (μm/ns) ΔU_{BO}	Transit Time (ns) Δt
s4075	Al	Al/MgO	523(+/-3)	6.11(+/-0.05)	4.79(+/-0.02)	5.25(+/-0.03)	-4.36(+/-0.02)	50.5(+/-0.2)
s4092	Al	Al/MgO	523(+/-2)	7.12(+/-0.05)	5.58(+/-0.03)	6.19(+/-0.03)	-5.08(+/-0.03)	48.5(+/-0.3)
s4104(a)	Ta	Ta/MgO	513(+/-2)	7.14(+/-0.05)	8.77(+/-0.04)	10.19(+/-0.05)	-8.16(+/-0.06)	39.4(+/-0.5)
s4104(b)	Ta	MgO/MgO	514(+/-4)	7.14(+/-0.05)	8.80(+/-0.04)	10.20(+/-0.05)	-8.19(+/-0.06)	39.8(+/-1.0)
s4108	Ta	MgO/MgO	387(+/-3)	6.25(+/-0.05)	7.77(+/-0.04)	8.92(+/-0.04)	-7.14(+/-0.04)	31.3(+/-0.5)

Table 2: Experimental results for the single shock case. The proposed method is compared with impedance matching results.

Shot Number	Shock Velocity (μm/ns) D	Shock Particle Velocity (μm/ns) U_P	Shock Pressure (GPa) P	Shock Density (g/cc) ρ	Shock Refractive Index n_S	
			This Method			
s4075	10.3(+/-0.1)	2.62(+/-0.02)	97(+/-1)	4.79(+/-0.02)	1.675(+/-0.006)	
s4092	10.8(+/-0.1)	3.06(+/-0.02)	118(+/-1)	5.00(+/-0.02)	1.672(+/-0.007)	
s4104(a)	13.0(+/-0.2)	4.85(+/-0.04)	226(+/-4)	5.71(+/-0.05)	1.659(+/-0.007)	
s4104(b)	12.9(+/-0.3)	4.86(+/-0.05)	225(+/-6)	5.74(+/-0.10)	1.657(+/-0.008)	
s4108	12.3(+/-0.2)	4.30(+/-0.04)	190(+/-4)	5.49(+/-0.06)	1.666(+/-0.007)	
Shot Number	Shock Velocity (μm/ns) D	Shock Particle Velocity (μm/ns) U_P	Shock Pressure (GPa) P	Shock Density (g/cc) ρ	Shock Refractive Index: Equation (1) n_S	Shock Refractive Index: Equation (2) n_S
			Impedance Matching			
s4075	10.2(+/-0.1)	2.62(+/-0.03)	95(+/-2)	4.82(+/-0.02)	1.674(+/-0.006)	1.674(+/-0.002)
s4092	10.8(+/-0.1)	3.07(+/-0.03)	119(+/-2)	5.00(+/-0.02)	1.673(+/-0.007)	1.672(+/-0.002)
s4104(a)	13.3(+/-0.1)	4.90(+/-0.03)	233(+/-7)	5.67(+/-0.03)	1.670(+/-0.007)	1.661(+/-0.004)
s4104(b)	13.3(+/-0.1)	4.90(+/-0.03)	233(+/-7)	5.67(+/-0.03)	1.666(+/-0.007)	1.659(+/-0.005)
s4108	12.4(+/-0.1)	4.29(+/-0.03)	191(+/-6)	5.46(+/-0.03)	1.664(+/-0.007)	1.667(+/-0.003)

Table 3: Measured parameters for the elastic-plastic two-wave structure.

Shot Number	Baseplate	Interface	Window Length (μm) L	Flyer Plate Velocity (μm/ns) U_{Flyer}	Apparent Velocity Overdriven Elastic Wave (μm/ns) $U_{App,I}$	Apparent Velocity Relaxed Elastic Wave (μm/ns) $U_{App,E}$	Apparent Velocity Elastic/Plastic Wave(μm/ns) $U_{App,P}$
s4081	Al	Al/MgO	532(+/-2.5)	4.06(+/-0.05)	2.78(+/-0.05)	NaN	3.16(+/-0.02)
s4122(a)	Al	Al/MgO	512(+/-5)	2.92(+/-0.05)	1.94(+/-0.01)	NaN	2.28(+/-0.03)
s4122(b)	Al	MgO/MgO	522(+/-3)	2.92(+/-0.05)	NaN	0.23(+/-0.1)	2.30(+/-0.02)

Shot Number	Baseplate	Transit Time (ns) Δt_E	Free Surface Velocity (μm/ns) U_{FS_E}	Discontinuity at Breakout (μm/ns) ΔU_{BO_E}	Transit Time (ns) Δt_P	Free Surface Velocity (μm/ns) U_{FS_P}	Discontinuity at Breakout (μm/ns) $\Delta U_{BO_{PE}}$
		Elastic Wave Conditions			Plastic Wave Conditions		
s4081	Al	54.1(+/-1.1)	0.30(+/-0.1)	-0.25(+/-0.1)	58.0(+/-1.9)	3.32(+/-0.1)	-2.59(+/-0.1)
s4122(a)	Al	52.2(+/-2.2)	0.21(+/-0.05)	-0.15(+/-0.05)	58.2(+/-5.1)	2.35(+/-0.05)	-1.95(+/-0.05)
s4122(b)	Al	54.2(+/-1.1)	0.15(+/-0.1)	-0.18(+/-0.1)	61.8(+/-2.5)	2.33(+/-0.1)	-1.89(+/-0.1)

Table 4: Experimental results for the elastic-plastic two-wave structure determined at breakout.

Shot Number	Shock Velocity (um/ns)	Particle Velocity (um/ns)	Refractive Index	Density (g/cc)	Pressure (GPa)
			Elastic Wave		
	D_E	$U_{True,E}$	n_{S_E}	ρ_e	P_e
s4081	9.8(+/-0.2)	0.15(+/-0.05)	1.713(+/-0.006)	3.64(+/-0.02)	5.3(+/-2.0)
s4122(a)	9.8(+/-0.4)	0.10(+/-0.03)	1.715(+/-0.003)	3.62(+/-0.01)	3.6(+/-1.0)
s4122(b)	9.6(+/-0.2)	0.08(+/-0.05)	1.711(+/-0.006)	3.61(+/-0.02)	2.6(+/-1.7)
			Plastic Wave		
	D_P	$U_{True,P}$	n_{S_P}	ρ_P	P_P
s4081	9.2(+/-0.3)	1.72(+/-0.04)	1.686(+/-0.008)	4.40(+/-0.04)	57(+/-6)
s4122(a)	8.8(+/-0.8)	1.21(+/-0.03)	1.689(+/-0.006)	4.15(+/-0.03)	38(+/-4)
s4122(b)	8.5(+/-0.3)	1.24(+/-0.04)	1.693(+/-0.008)	4.19(+/-0.04)	38(+/-3)
			Elastic-Plastic Wave		
	D_{PE}	$U_{True,PE}$	$n_{S_{PE}}$	ρ_{PE}	P_{PE}
s4081	10.1(+/-0.2)	1.66(+/-0.07)	1.689(+/-0.008)	4.22(+/-0.06)	NaN
s4122(a)	10.0(+/-0.4)	1.18(+/-0.04)	1.691(+/-0.006)	4.01(+/-0.03)	NaN
s4122(b)	9.8(+/-0.2)	1.16(+/-0.05)	1.695(+/-0.008)	4.03(+/-0.06)	NaN
			Over-Driven Elastic Wave*		
	D_I**	$U_{True,I}$	n_{S_I}	ρ_I	P_I
s4081	9.696	1.63(+/-0.05)	1.718(+/-0.011)	4.31(+/-0.02)	57(+/-2)
s4122(a)	9.696	1.11(+/-0.03)	1.710(+/-0.006)	4.04(+/-0.02)	38(+/-2)

*Values determined from impedance matching
** Elastic wave ultra-sonic measured value[21]